nature energy

SUPPLEMENTARY INFORMATION

https://doi.org/10.1038/s41560-018-0086-3

In the format provided by the authors and unedited.

Thermoelectric properties and performance of flexible reduced graphene oxide films up to 3,000 K

Tian Li[1], Andrea D. Pickel[2], Yonggang Yao[1], Yanan Chen[1], Yuqiang Zeng[3], Steven D. Lacey[1], Yiju Li[1], Yilin Wang[1], Jiaqi Dai[1], Yanbin Wang[1], Bao Yang[4], Michael S. Fuhrer[5], Amy Marconnet[3], Chris Dames[2,6], Dennis H. Drew[7]* and Liangbing Hu[1]*

[1]Department of Materials Science and Engineering, University of Maryland College Park, College Park, MD, USA. [2]Department of Mechanical Engineering, University of Berkeley, Berkeley, CA, USA. [3]School of Mechanical Engineering, Purdue University, West Lafayette, IN, USA. [4]Department of Mechanical Engineering, University of Maryland College Park, College Park, MD, USA. [5]School of Physics and Astronomy, and Monash Centre for Atomically Thin Materials, Monash University, Monash, VIC, Australia. [6]Materials Sciences Division, Lawrence Berkeley National Laboratory, Berkeley, CA, USA. [7]Department of Physics, University of Maryland College Park, College Park, MD, USA. *e-mail: hdrew@physics.umd.edu; binghu@umd.edu

Supplementary Information

Supplementary Discussion 1: Bandgap measurement of HT-RGO

Compared to conventional thermal reduction in a furnace, Joule heating is advantageous due to the rapid heat treatment that reaches significantly higher temperatures. The reduction temperature of the RGO film can be controlled by simply adjusting the magnitude of the DC current. Four-probe measurements of longitudinal resistivity ρ_{xx} and Hall resistivity ρ_{xy} of the RGO film were conducted by lock-in techniques at a low frequency of 3.7 Hz in a commercial cryostat (Quantum Design PPMS-9). The Hall voltage was recorded in both polarities of the magnetic field and anti-symmetrized to remove longitudinal voltage components.

The charge transport behavior in the *RGO* film can be described by a combination of Mott variable range hopping (VRH), Arrhenius thermal activation and quantum tunneling,[32-40] as shown in Eq. 1:

$$G(T) = G_h \exp(-(\frac{T_0}{T})^{\frac{1}{4}}) + G_a \exp(-\frac{T_a}{T}) + \mathrm{G}_t \qquad \text{(Supplementary Equation 1.1)}$$

where G_h, G_a and G_t are the contributions of Mott-VRH, thermal activation, and quantum tunneling, respectively; T_0 and T_a are the characteristic temperatures for Mott-VRH and thermal activation. The temperature dependence of conductivities for the RGO films are shown in Supplementary Figure 1 and fit well with Eq. S1. The charge transport in 1000 K RGO film is dominated by Mott-VRH, and the thermal activation and quantum tunneling mechanisms start to have contributions as the reduction temperature increases. $k_B T_a$ in the thermal activation mechanism indicates an energy barrier (i.e. bandgap, $\mathrm{E_g}$), where carriers can be thermally excited to the conduction band. The bandgaps for the 1000 K and 3000 K RGO films can thus be fitted, as shown in Supplementary Figure 1 (a-b).

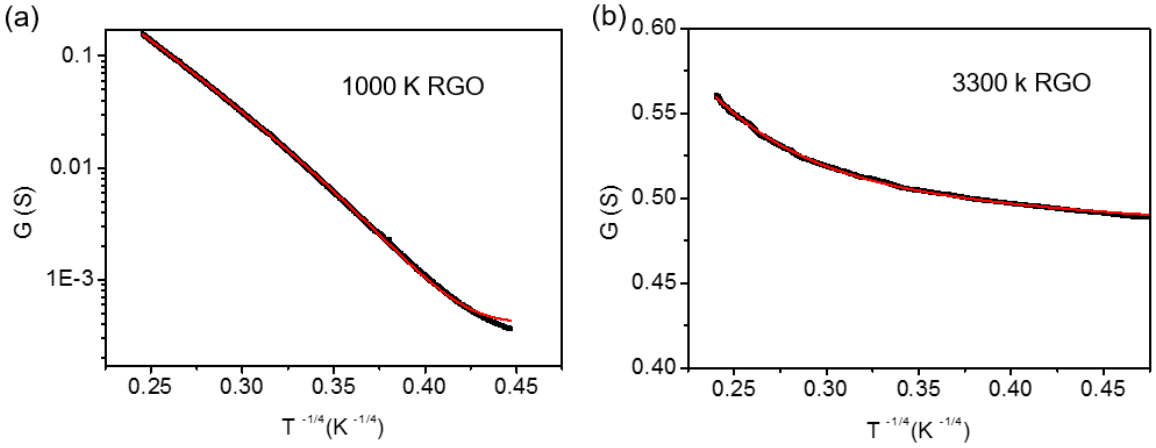

Supplementary Figure 1. Conductivities, σ, of the (a) ~1000 K and (b) ~3300 K-reduced RGO films versus $T^{-1/4}$ (black lines) and their fitting to Eq. S1.1 (red lines), which represents a 3D variable-range hopping in parallel with thermal activation and quantum tunneling. The bandgaps for the 1000 K and 3000 K RGO films are 6 meV, and 1 meV, respectively. This plot shows the mathematical fitting with the experimental obtained conductance (> 97% confidence band).

Supplementary Discussion 2: Preparation and characterization of HT-RGO

Well-dispersed GO nanosheets were prepared by the modified Hummer's method with a concentration of 3 mg/mL in deionized (DI) water (Figure 2a, S1)[32]. The GO films were fabricated by either vacuum filtration or three-dimensional (3D) printing with an aqueous GO solution (Figure 2b, S2). The typical GO nanosheet thickness (0.9 nm) was determined by atomic force microscopy (AFM) as shown in Supplementary Figure 3a. The as-prepared GO film was initially reduced at 1000 K in a tube furnace under an argon atmosphere to achieve a high electrical conductivity throughout the entire sample. This electrically conductive RGO film was subsequently Joule-heated to a temperature of 2000 K - 3300 K by adjusting the input current. Figure 2a demonstrates that the HT-RGO film (thickness: 3.5 μm) is mechanically flexible. The 3300 K HT-RGO has a much smoother surface compared to the 1000 K RGO (Supplementary Figure 3b). High-resolution scanning electron microscopy (SEM) images of the HT-RGO film indicate that the RGO nanosheets are aligned in-plane and have a well-defined layered structure (Figure 2b). High temperature annealing at 3300 K also leads to a highly crystalline structure in the resultant HT-RGO film (Supplementary Figure 3c).

Hall effect measurements were employed to characterize the in-plane electrical properties of the RGO films prepared by different reduction temperatures. The measurements confirmed that the majority charge carriers are holes, corresponding to a *p*-type material. The electrical conductivity ($\sigma = pe\mu$) increases from ~5 S/cm for a 1000 K RGO film to 1450 S/cm for a 3300 K RGO (Figure 2c). Note that the measured conductivity is stable at a given T, which eliminates the possibility of ionic conductivity effects in the observed thermopower. The hole mobility (μ) increases in a similar manner when the reduction temperature increases. This is likely due to significant removal of impurities and improved crystallinity of the RGO sheets via high temperature annealing (Figure 2d). The hole density per atomic layer (*p*) for RGO decreases slightly at higher temperatures with a value on the order of 10^{12} cm^{-2} (Figure 2d). After the RGO ribbon is treated at 3300 K, the *p* dopants are atomically stable over a broad temperature range.

We further investigated the structure and functional groups of RGO reduced at 1000 K and 3300 K via Raman spectroscopy and X-ray diffraction (XRD) (Figure 2e-f). Compared to the 1000 K

RGO, the 3300 K RGO has a much smaller D peak centered at ~1350 cm^{-1} and a more pronounced 2D peak at ~2690 cm^{-1}. The intensity ratio of D to G peaks (I_D/I_G) significantly decreased from 1.11 to 0.08, which indicates a predominantly sp^2-bonded carbon structure with a decreased defect density due to the higher reduction temperature. The linewidth of the G peak narrows from 335 cm^{-1} to 122 cm^{-1} as the reduction temperature increases from 1000 K to 3300 K. Additionally, the 3300 K GO displays a sharp 2D peak with a linewidth of 155 cm^{-1}, which confirms its highly crystalline structure. The high I_{2D}/I_G value and the sharp 2D band with a single Lorentzian peak demonstrates that the obtained 3300 K RGO film is primarily composed of stacked single layer graphene sheets (Supplementary Figure 3e). After the 3300 K thermal reduction, the (002) XRD peak (at 26.46°) is present, which is characteristic of graphite (Figure 2f). Based on the position of this sharp peak, the RGO interlayer distance was determined to be ~0.336 nm, which is in good agreement with the interlayer spacing of graphite (~0.334 nm). For comparison, the characteristic peak for RGO reduced at 1000 K is much broader and corresponds to a larger interlayer spacing. Supplementary Figure 3f shows the C1s core levels of RGO reduced under different conditions. The X-ray photoemission spectroscopy (XPS) data for the 3300 K RGO exhibits a single C1s peak with a full width at half maximum (FWHM) around 0.607 eV. This is substantially smaller than the 1000 K RGO film (FWHM of 1.05 eV), which corresponds to a smaller number of sp^3 hybridized bonds after the reduction process[33].

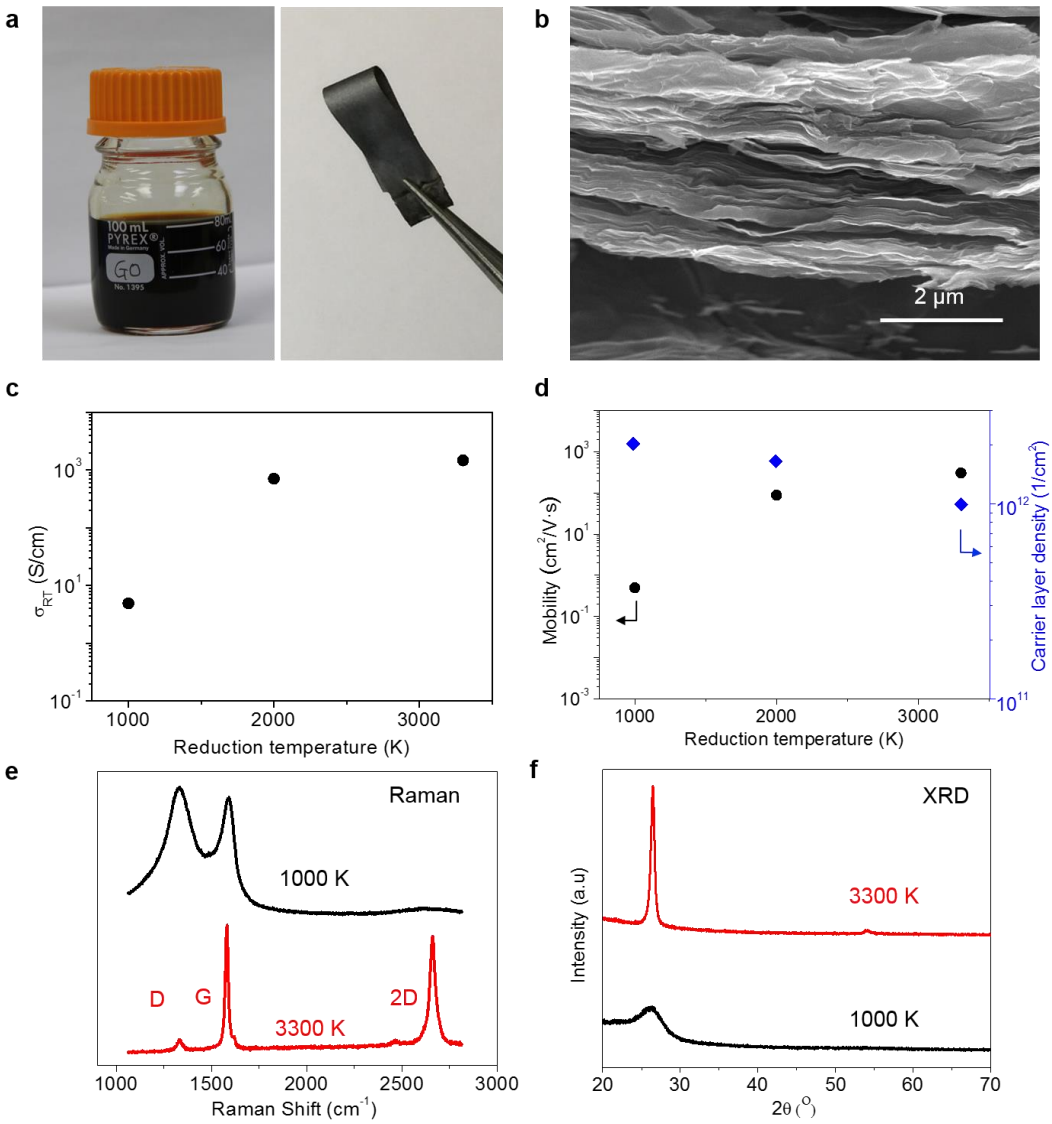

Supplementary Figure 2. The effect of high temperature reduction on RGO. (a) Digital image of well-dispersed GO nanosheets in DI water, which is used to fabricate flexible GO films. After thermal treatment at 1000 K and subsequent high temperature reduction via joule heating at 3300 K, the freestanding 3.5 μm thick HT-RGO films remain mechanically strong and flexible. (b) Cross-sectional SEM image of a HT-RGO film with a layered structure, where the RGO nanosheets are oriented in the planar direction. (c) Room temperature electrical conductivity obtained from Hall measurements for Joule heated RGO films annealed at different temperatures. (d) Mobility and carrier density per layer for (*p*-type) RGO annealed at different temperatures. While there is a dramatic increase in carrier mobility (from 5 $cm^2/V·s$ to ~300 $cm^2/V·s$**)**, the carrier density per layer decreases to ~10^{12} cm^{-2}. (e) Raman spectroscopy of RGO films reduced at 1000 K and 3300 K, respectively. The high temperature reduction leads to crystalline graphene with a pronounced 2D peak and a small D-to-G intensity ratio. (f) XRD of RGO films reduced at 1000 K and 3300 K, respectively, which further confirms how high temperature reduction improves crystallinity.

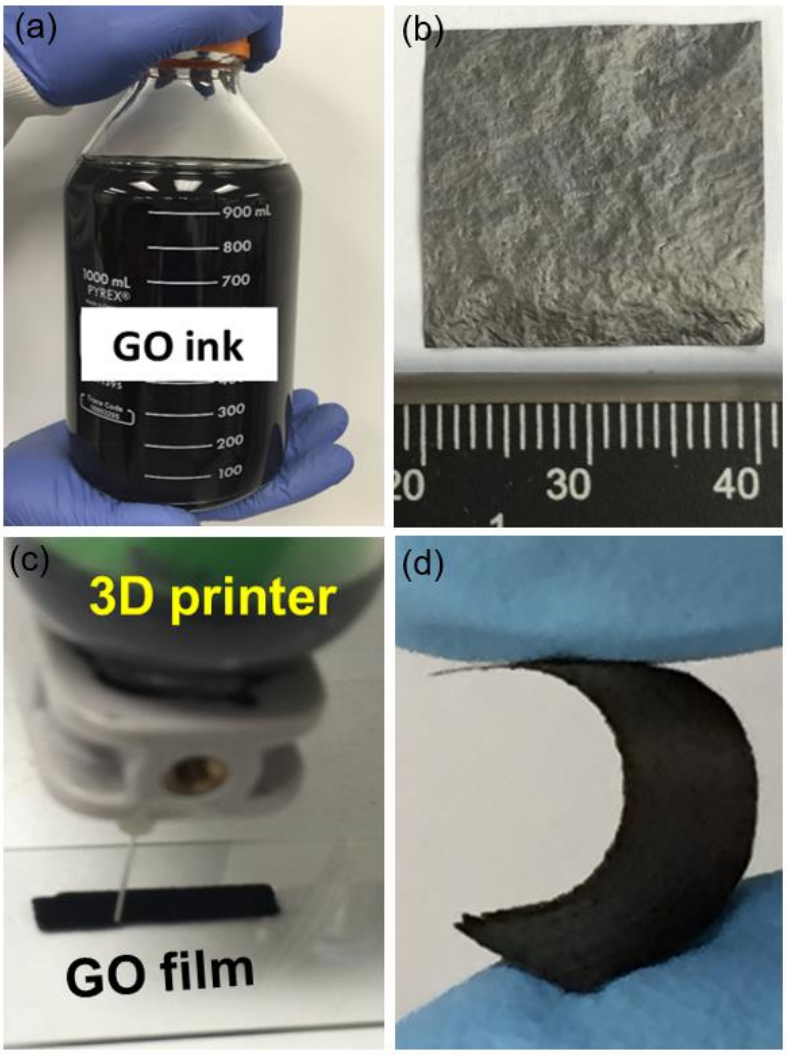

Supplementary Figure 3: (a) Digital images of a 1 L bottle of graphene oxide (GO) ink and (b) a large-area RGO film. (c) Digital images of the GO film being 3D printed as well as (d) the excellent flexibility of the 3D printed GO film.

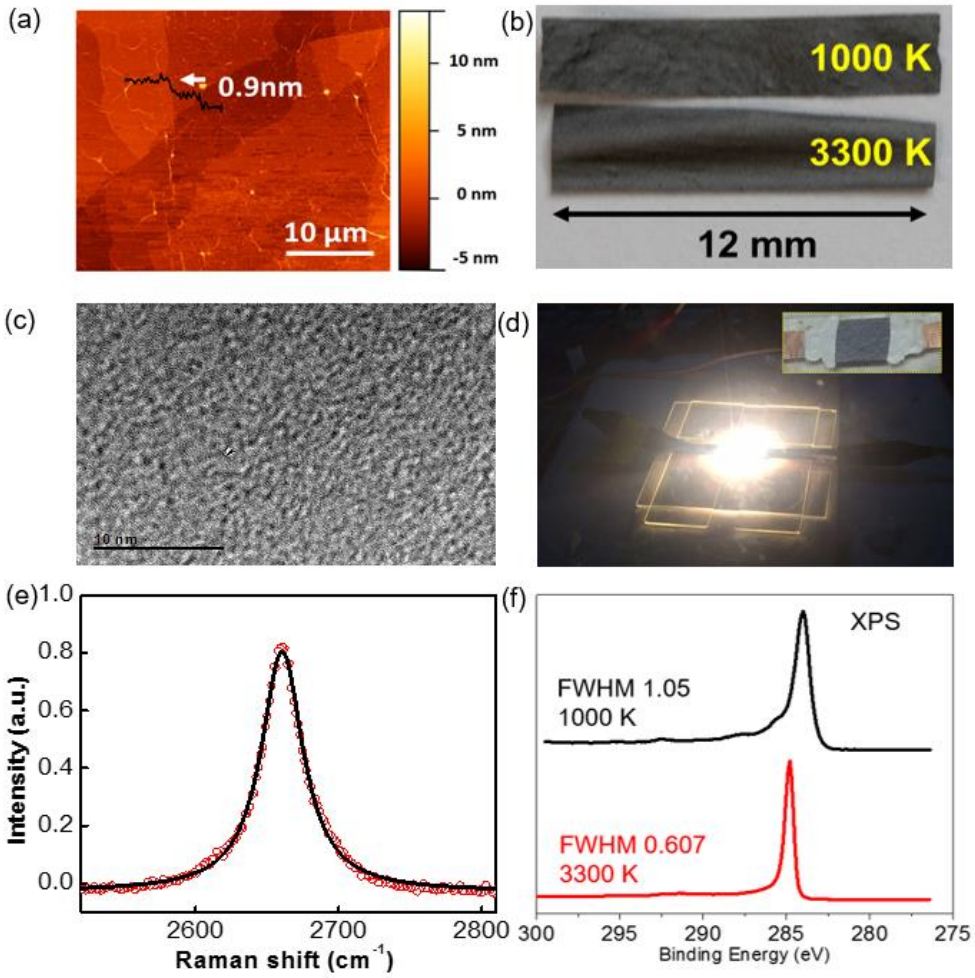

Supplementary Figure 4: Material characterization of HT-RGO: (a) Atomic force microscopy (AFM) image of GO nanosheets with a thickness of 0.9 nm, which indicates predominantly monolayer GO nanosheets. (b) Digital image of a 1000 K and 3300 K annealed RGO film. The 3300 K RGO film is visibly smoother than the 1000 K RGO film. (c) TEM image of the 3300 K RGO film. The lattice fringes reveal the 3300K RGO film's highly crystalline graphene-like structure. The scale bar represents 10 nm. (d) An incandescent 1 cm × 1 cm RGO film during operation (i.e. under an electrical bias). Due to its high temperature, the film starts to emit white light. The inset is a digital image of the tested film with both copper tape and silver paste electrical connections. (e) Raman spectra for the 3300 K RGO film's 2D band (red open circles). The solid black line is a Lorentzian fit to the RGO data, indicating that the RGO film is composed of high-quality monolayer graphene nanosheets with random stacking. (f) XPS data of RGO films reduced at 1000 K and 3300 K, respectively. The FWHM (full width half maximum) for the 1000 K RGO and 3300 K RGO films are 1.05 eV and 0.607 eV, respectively.

Supplementary Discussion 3: Modeling of HT-RGO thermoelectrics

After the 3300 K treatment, the RGO ribbon exhibits graphene-like characteristics. The 3300 K RGO film consists of a stack of graphene flakes with numerous boundaries between them. Thus, we have modeled the thermoelectric performance of the 3300 K RGO film as if it were graphene. The following assumptions were made: (1) the material's conductivity has a linear relationship with carrier density and (2) the carrier density consists of the doping-induced carrier density and the thermally-induced carrier density:

$$\sigma = (n^2 + n_T^2)^{1/2} e\mu \qquad \text{(Supplementary Equation 2.1)}$$

where $n = \frac{k_B^{\,2}}{\pi} = \left(\frac{E_F}{\hbar v_F}\right)^2 \frac{1}{\pi}$ and $n_T = \frac{\pi (k_B T)^2}{6\hbar^2 v_F^{\,2}}$ are from the graphene model and v_F is the Fermi velocity.

The electrical conductivity can be rewritten as:

$$\sigma = \left(\frac{k_B^{\,2}}{\pi\hbar^2 v_F^{\,2}}\right)\left(T_F^4 + \frac{\pi^4 T^4}{36}\right)^{1/2} e\mu \qquad \text{(Supplementary Equation 2.2)}$$

From the Wiedemann–Franz law and the Mott relation, the thermopower can be written as:

$$S = -\frac{\Lambda e T}{k_B}\frac{d\ln\sigma}{dT_F} = -\frac{\Lambda e T}{k_B}\frac{2T_F^3}{\left(T_F^4 + \frac{\pi^4 T^4}{36}\right)} = -\frac{2\Lambda e}{k_B}\frac{T}{T_F}\frac{1}{\left(1 + \frac{\pi^4}{36}\frac{T^4}{T_F^4}\right)}$$

(Supplementary Equation 2.3)

where Λ is the Sommerfeld value of the Lorenz number, 2.44 x 10^{-8} V^2K^{-2}.

When $T \ll T_F$:

$$S = -\frac{2\Lambda e}{k_B}\left(\frac{T}{T_F}\right) \qquad \text{(Supplementary Equation 2.4)}$$

When $T \gg T_F$:

$$S = -\frac{\Lambda e}{k_B}\left(\frac{T_F^3}{T^3}\right)\frac{72}{\pi^4} \qquad \text{(Supplementary Equation 2.5)}$$

The maximum figure of merit *ZT* (assuming zero lattice thermal conductivity), thermopower *S*, thermoelectric voltage *V* (referenced to T_{cold} = 300 K), and electrical conductivity σ are shown as functions of temperature in Supplementary Figure 4. Notably, the *ZT* and *S* curves show a peak at approximately $T = 0.59T_F$, where $S_{peak} \sim 250$ μV/K and $ZT_{peak} \approx 2.6$.

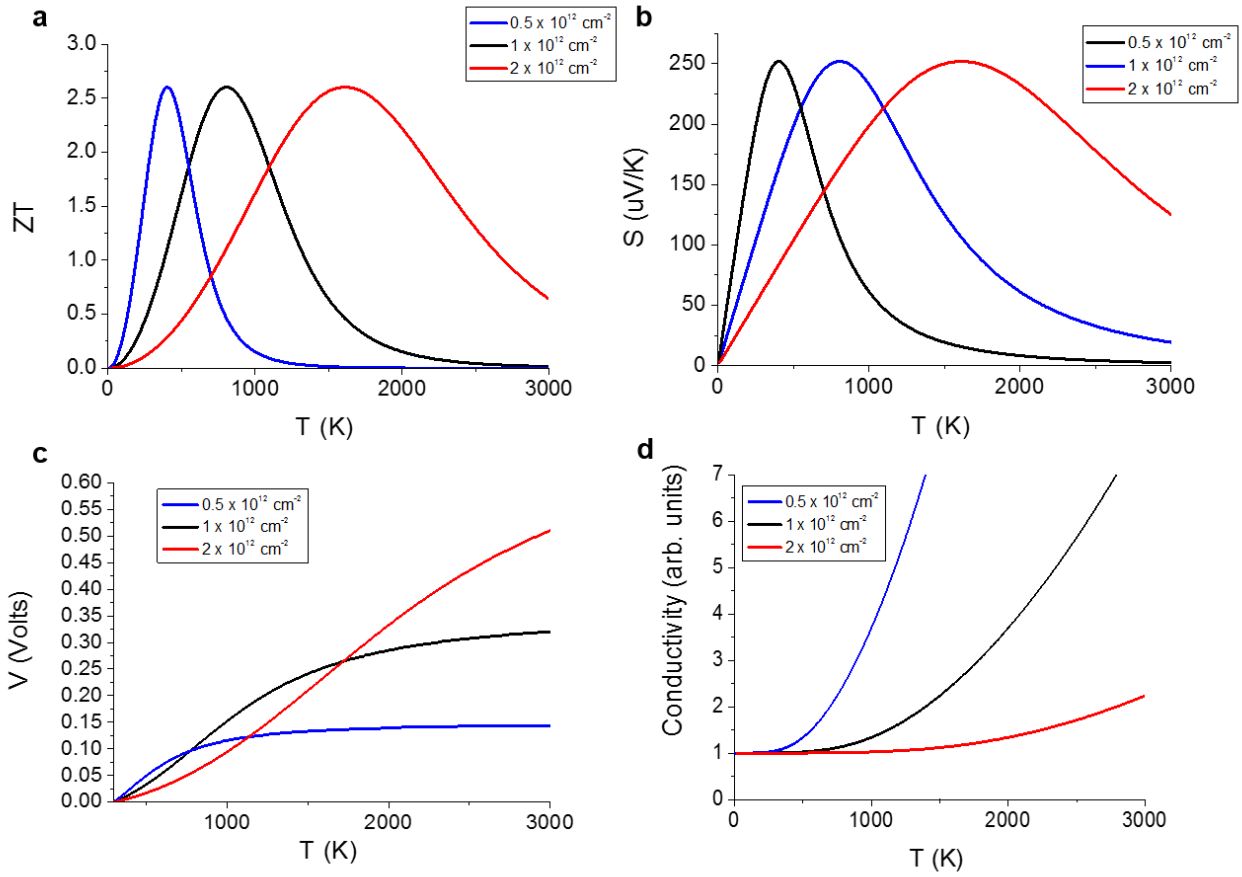

Supplementary Figure 5. Simulation results for RGO's thermoelectric performance as a function of doping level obtained via the graphene model. (a) Maximum *ZT* achievable if the phonon thermal conductivity is zero. (b) The Seebeck coefficient initially increases linearly at low temperature, reaches a peak value of 250 μV/K, and then decreases as $1/T^3$. The peak temperature for *ZT* and the Seebeck coefficient can be tuned with doping level. Peak thermoelectric performance shifts to higher temperatures with higher doping levels. (c) The maximum achievable thermoelectric voltage with different doping levels based on the Seebeck coefficient calculated in (b). The thermoelectric voltage starts to saturate at elevated temperatures, consistent with experimental observations in Fig. 4a of the main text. (d) The electrical conductivity increases due to the thermal excitation of carriers. Note that doping levels are indicated in the legends.

Supplementary Discussion 4: Electrical conductivity of HT-RGO from 300 K to 3000 K

The measurement data from 300 K to 1100 K was taken in a conventional oven with 90% N_2 and 10% H_2 flow (to further reduce O_2 pressure). The oven has a four-wire feed-through connecting the Keithley 2400 source meter. The RGO ribbon was fixed to a ceramic stand. Silver paste and silver wires were used to connect four spots of the RGO ribbon to the electrical feed-through of the oven. A thermocouple was placed close to the center of the RGO ribbon to monitor the temperature *in-situ*. The measurement data from 1400 K to 3000 K was done in a vacuum chamber with a Joule heated RGO ribbon via a four-probe scheme as well. Note that the error bar results from sample variation and temperature non-uniformity within the middle of the two tungsten probes. At higher operation temperatures, the temperature variation in the middle of the RGO ribbon reduces, which leads to lower error bars. Each HT-RGO ribbon was treated at a high temperature of >3000 K. The temperature during treatment was monitored by spectral fitting and controlled via self-Joule-heating. To ensure uniformity, each sample was re-treated at least 3 times during the annealing process. The RGO ribbon was detached and reattached with conductive paste for subsequent treatments. The electrical current was slowly raised to the desired value while using the radiation spectral fitting to monitor the radiation temperature.

Supplementary Discussion 5: Thermal conductivity measurement from 300 K to 630 K

(a) Four-probe electrothermal measurement

A vacuum chamber with a four-point probe setup and temperature-controlled thermal stage was used (Supplementary Figure 6a). The RGO film serves as both the heater and thermometer during the measurement. The RGO film suspended above the substrate was Joule heated via an applied current. Assuming negligible convective and radiative heat losses, the governing equation for one-dimensional heat conduction in the suspended RGO film is given as:

$$kA\frac{d^2T}{dx^2} + I^2\frac{R}{L} = 0 \qquad \text{(Supplementary Equation 3.1)}$$

$$T(x = \pm L/2) = T_0 \qquad \text{(Supplementary Equation 3.2)}$$

where k is the thermal conductivity of the RGO film, I is the applied electrical current, R is the electrical resistance, T_0 is the temperature of the stage, A is the cross-sectional area, and L is the length of the suspended RGO film. The temperature can be represented as:

$$\Delta T(x) = T(x) - T_0 = -\frac{I^2R}{2kAL}x^2 + \frac{I^2RL}{8kA} \qquad \text{(Supplementary Equation 3.2)}$$

Note that this equation describes the relationship between the temperature profile and the thermal conductivity of the RGO film. The average temperature rise along the film is given by:

$$\Delta\bar{T} = \int_{-L/2}^{L/2}\Delta T(x)dx / L = \frac{I^2RL}{12kA} \qquad \text{(Supplementary Equation 3.3)}$$

Note that a simple solution is obtained by assuming constant electrical resistance during the heating process, which is valid only when the variation is small compared to the electrical resistance at the reference temperature T_0. Our measurements show a linear temperature dependence in terms of electrical conductivity (Supplementary Figure 6(b)). *1/R(T)* varies linearly with the temperature as follows:

$$\frac{1}{R(T)} = aT + b \qquad \text{(Supplementary Equation 3.5)}$$

where a and b are coefficients determined by the fitting to *1/R(T) vs T*. The corresponding temperature rise can be calculated based on the measured electrical resistance as:

$$\frac{1}{R(T)} - \frac{1}{R(T_0)} = a(T - T_0) \qquad \text{(Supplementary Equation 3.6)}$$

and thus the temperature rise is determined by:

$$\Delta T = T - T_0 = -\frac{R(T) - R(T_0)}{aR(T)R(T_0)} = -\frac{\Delta R}{aR(T)R(T_0)} \quad \text{(Supplementary Equation 3.7)}$$

Therefore, the solution of the thermal conductivity is:

$$k = -\frac{aLI^2 R(T_0) RR(\bar{T})}{12A\Delta R} \quad \text{(Supplementary Equation 3.8)}$$

The uncertainty due to the simplified solution is analyzed by calculating the thermal conductivity with R from $R(T_0)$ to $R(\bar{T})$. The electrical resistance (ΔR) as a function of I^2 is shown in Supplementary Figure 5(c). The obtained thermal conductivity is shown in Supplementary Figure 7 from 294 K to 650 K.

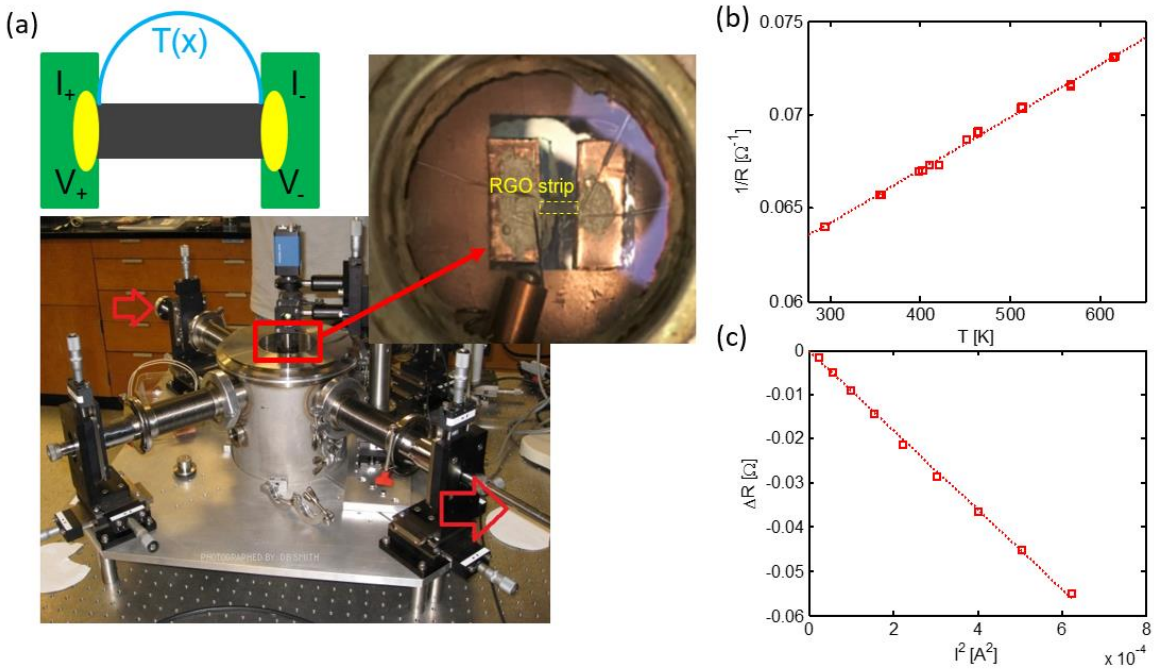

Supplementary Figure 6. (a) Four-probe measurement using a high temperature probe station. (b) The RGO film exhibits a linear temperature dependence from 294 K to 650 K. (c) The change in electrical resistance (ΔR) as a function of I^2. ΔR is proportional to the average temperature rise in the sample and I^2 is proportional to the power dissipation. Thus, the slope of this curve corresponds to the thermal resistance of the sample.

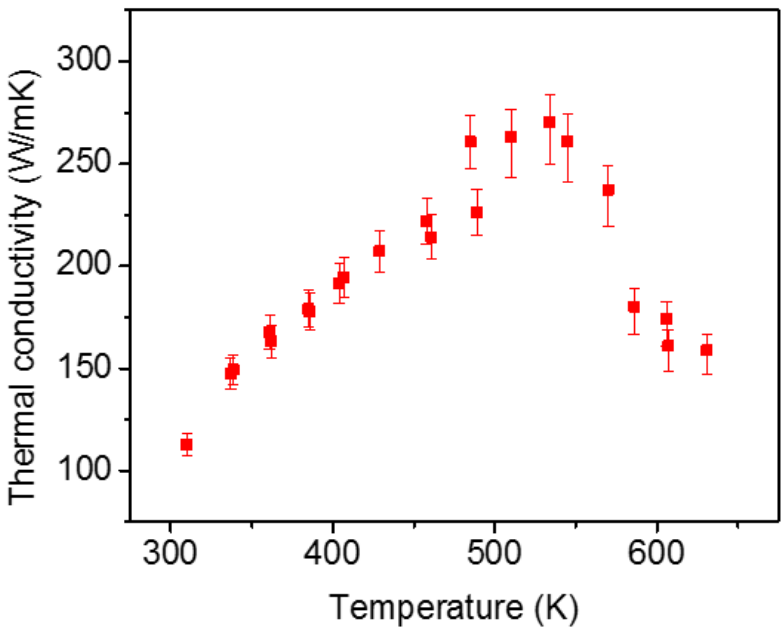

Supplementary Figure 7. Thermal conductivity as a function of operation temperature for an RGO film annealed at 3000 K. Please refer to the text for the definition of the error bars.

To further verify the obtained thermal conductivity, a separate sample was measured using a steady state Joule heating technique, where an IR microscope measured the steady state temperature profile within the sample. Similar to the setup shown in Supplementary Figure 6, current flows through a suspended RGO sample. The IR microscope measures the two-dimensional temperature profile within the film (Supplementary Figure 8(a)). As the sample is suspended in air for this measurement, note that a model that includes both the conduction within the film and convection losses to the surroundings is required to extract the thermal conductivity from the temperature profile. An example fit is shown in Supplementary Figure 8(b), where both thermal conductivity and the convection loss coefficient h are measured. Supplementary Figure 8(c) summarizes the data from the different temperature profiles. The results are in good agreement with the data measured with the four-probe method (Supplementary Figure 8(d)).

In the four-probe electrothermal measurement, uncertainty in the measured thermal conductivity was analyzed by fitting to ΔR vs I^2 with the variations in the different input parameters. The length, width, and thickness of the samples were assumed to be accurate within ±0.1%, ±0.1%, and ±1.0%, respectively. The variation of resistance was within ±0.25% and the fitted parameter

a was estimated to be accurate within [-2.5%, +1.0%]. As for the IR microscopy measurement, a similar method was used to calculate the uncertainty of the thermal conductivity by fitting to the analytical solution. The uncertainty contribution from the heat convection was determined by repeated measurements.

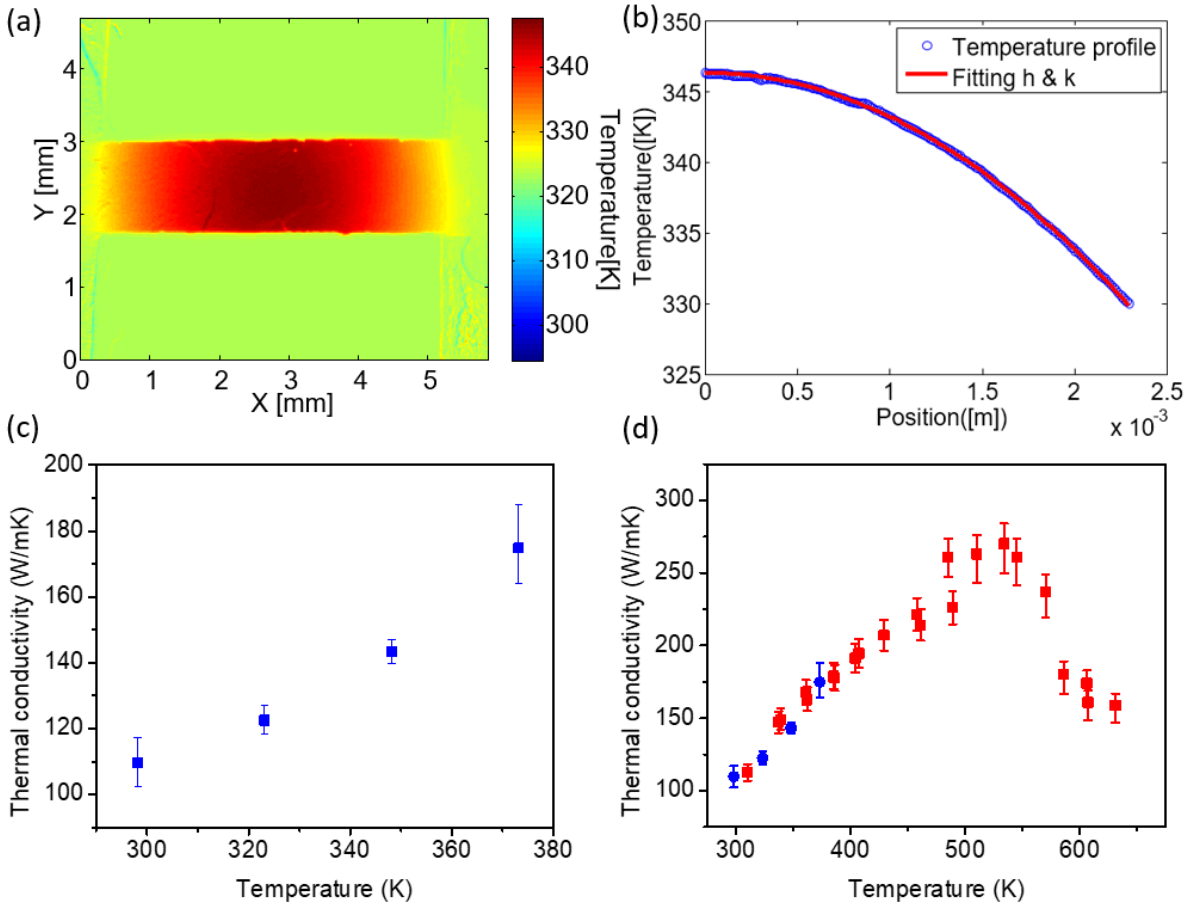

Supplementary Figure 8. (a) Infrared microscopy thermal map of a RGO film during the steady state Joule heating experiments. (b) The 1D profile is extracted by averaging each column of pixels within the film and recognizing symmetry at the center plane of the strip. The red line shows the best fit of a model including convection and conduction within the system. (c) Thermal conductivity of the RGO film from the IR microscopy method. Please refer to the text for the calculation of the error bars. (d) Comparison of the four-probe electrothermal measurement and the IR microscopy measurement, which shows good agreement between the measured values. Please refer to the text for the calculation of the error bars.

Supplementary Discussion 6: Analyzing the thermal conductivity of HT-RGO ribbon under high temperature operation (>1200 K)

We are unaware of any standard measurement method suitable under ultra-high temperatures. Consequently, we developed our own method since both of the aforementioned low-*T* methods become infeasible due to: (1) the strong T^4 scaling of radiation; (2) surface heat losses from the RGO ribbon, which become critical at high temperature and cannot be accounted for using the resistance thermometry approach; (3) the dominant wavelengths of thermal emission are shifted closer to the visible range, which is outside the wavelength range for which IR photodetectors are optimized; (4) the magnitude of the infrared radiation emitted within the IR detector wavelength range saturates this detector. An additional challenge is the large temperature variation along the Joule heated RGO ribbon, which violates the linearized, constant parameter model used in the standard fitting approach. Therefore, our method builds upon previously developed methodologies[34]. Specifically, it generalizes the IR microscope $T(x)$-fitting approach into the visible wavelength regime, while incorporating temperature-dependent properties into a non-linear multimode heat transfer model.

In order to evaluate the approximate range of thermal conductivity values under high temperature operation, we Joule-heated a pre-annealed RGO ribbon and recorded the illumination intensity profile over a range of operation temperatures. A 550 nm bandpass filter was used in conjunction with a camera to capture the images shown in Supplementary Figure 8. The intensity profile can be converted to a temperature profile by fitting the emission spectrum with the Planck function[34].

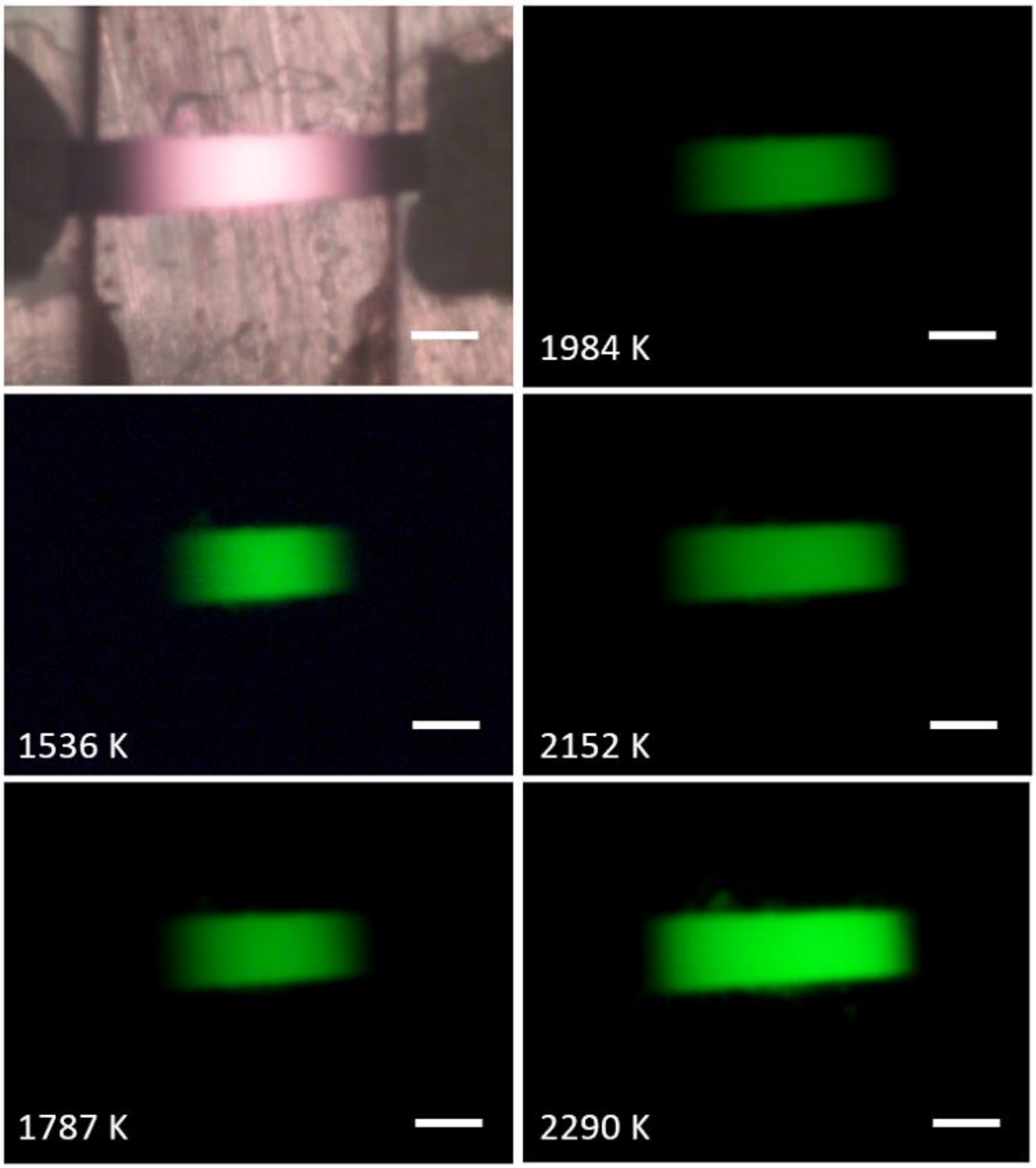

Supplementary Figure 9. A RGO ribbon with the dimension of 3 mm × 0.5 mm × 3.5 μm (length × width × thickness) was used for taking the thermal images. Thermal images taken with a 550 nm bandpass filter for the same RGO ribbon heated to different temperatures (different exposure time was chosen to ensure no intensity saturation). The temperature is obtained separately by fitting the emission spectrum with the Planck function. These intensity profiles can also be related to the thermal conductivity. Scale bar: 0.5 mm.

a) Numerical Solution of the Governing Differential Equation

In order to model the temperature distribution in the Joule heated RGO strips, we developed a non-linear thermal model closely following our previous work[34]. We modeled the RGO strip as a long fin with non-uniform volumetric generation and surface radiation losses, which can be described by the governing differential equation:

$$\frac{d}{dx}k\left(\frac{d\theta}{dx}\right) + g - \frac{h_{rad}\theta}{\delta_c} = 0 \qquad \text{(Supplementary Equation 4.1)}$$

Here, $\theta(x) = T(x) - T_\infty$, $g(T)$ is the non-uniform volumetric power generation due to the temperature-dependent resistivity $\rho(T)$. Other parameters such as the thermal conductivity $k(T)$ and the characteristic thickness δ_c, which we define as the ratio of the volume to the surface area, are important. $h_{rad} = \varepsilon\sigma(T^2 + T_\infty^2)(T + T_\infty)$ is the radiative heat transfer coefficient, where σ is the Stefan-Boltzmann constant and $T(x)$ and T_∞ are the temperatures of the sample and the surroundings, respectively. We obtain the $\rho(T)$ function from a linear fit to the experimental $\sigma(T)$ data shown in Figure 3d. We then impose the boundary conditions: $T(x = \pm L) = T_\infty$. Here we assume a gray emissivity of ε = 0.8. Although the measured spectral absorbance data for the visible and near-infrared ranges (Figure 4d) does show a moderate decreasing trend, the effect of this wavelength dependence on the modeled temperature profile should be much less significant than the strong nonlinearities introduced by the temperature-dependent h_{rad} and k functions. Since h_{rad}, k, and g are all temperature-dependent, Eq. (S4.1) is a nonlinear equation with no closed-form analytical solution. Consequently, we solve this equation using an iterative finite-difference method.

b) Converting Between Intensity and Temperature

The solutions of Eq. (S4.1) are temperature profiles, while our raw experimental data are intensity profiles of the incandescent RGO. Supplementary Figure 10 shows a high dynamic range (HDR) image of a Joule heated sample with a peak temperature of approximately 2290 K and the corresponding intensity profile we obtained. To convert between intensity and temperature, we integrated the Planck distribution between 548 nm and 552 nm to represent the 550 nm bandpass filter used in our experiments[34]. The resultant integrated intensity in this regime is exponential with T^{-1}. Here, we use an experimentally determined emissivity based on

the measured absorbance data in the visible wavelength range (Figure 4d). We can then use this relationship to convert the measured intensity profiles into temperature profiles (or vice versa).

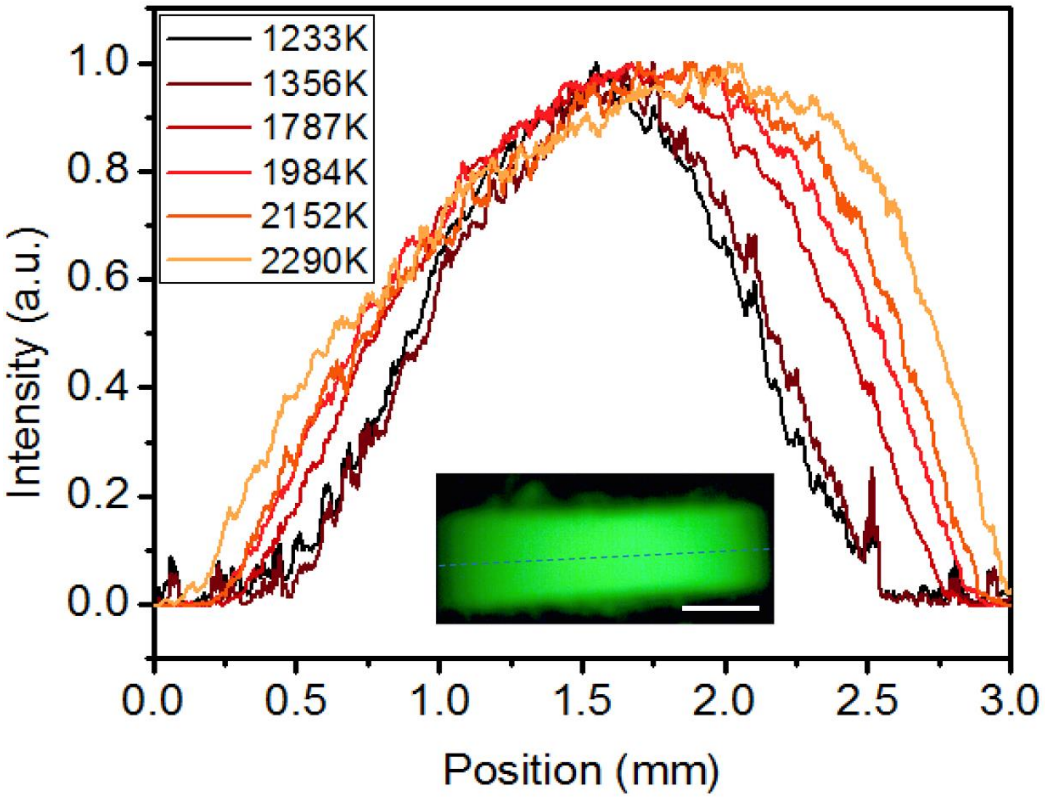

Supplementary Figure 10. The intensity profile along the centerline of the sample (the dashed line shown on the inset image) when heated to different temperature. The inset shows a high dynamic range (HDR) image of an incandescent RGO ribbon at 2290 K, constructed from multiple images of the same sample taken with different exposure times. Scale bar: 0.5 mm. The incandescent RGO appears green because of the 550 nm bandpass filter used when taking the images.

When we convert from intensity to temperature via the bandpass integrated Planck distribution, the initial T(x) result has the correct relative scaling but must be anchored using a known temperature value (e.g. the peak or endpoint temperature) in order to be interpreted on an absolute temperature scale. Note that it is the relative temperature variation along the RGO ribbon which is the most important aspect for our thermal conductivity fitting method, although due to the non-linear nature of the heat transfer problem the absolute temperature values are also needed. Supplementary Figure 11 compares the modeled peak temperature values obtained by

solving Eq. (S4.1), with the T_{peak} obtained from the Planck spectral fitting method (Eq. (1) of the main text), for six different Joule heating currents. The black dashed line indicates the ideal scenario, in which there is a one-to-one correspondence between the modeled peak temperatures and those obtained via spectral fitting. We observe that all the points lie close to this line, indicating that the two sets of temperature values are in good agreement. We also note that at high temperatures, where radiation losses dominate over conduction heat transfer, the peak temperature is independent from the thermal conductivity. Therefore, in this limit, we cannot draw any conclusions about the validity of the fitted thermal conductivity values based on the good agreement between the modeled peak temperatures and those extracted via spectral fitting. However, at lower temperatures where conduction remains significant, this agreement provides some additional indication that the fitted thermal conductivity values are reasonable. Empirically, we observe that for the lower three experimental Joule heating currents, the modeled peak temperature shows some sensitivity to the high temperature phonon thermal conductivity function. In contrast, the higher three input currents are insensitive to this parameter.

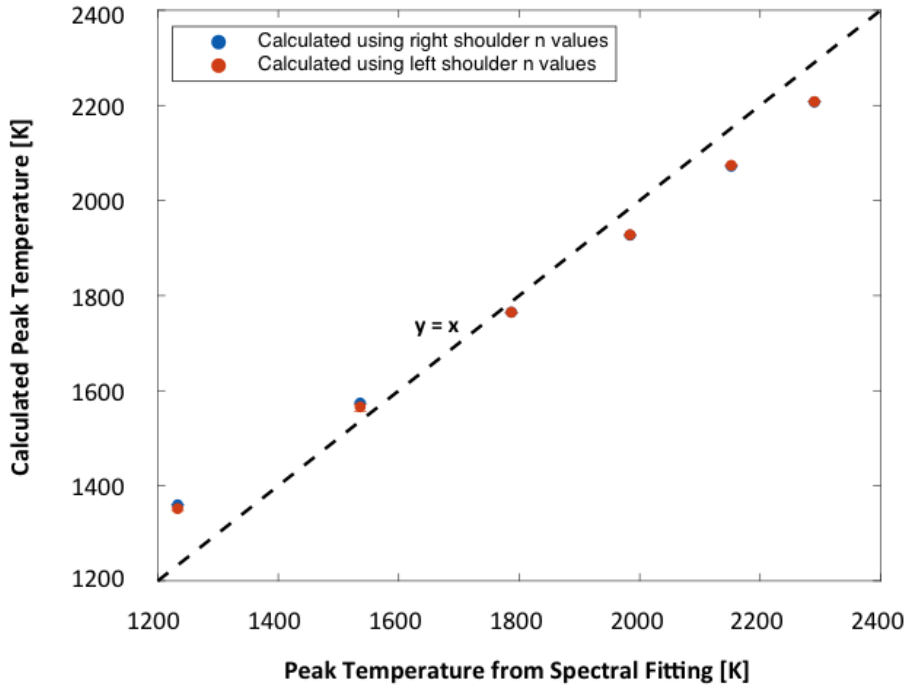

Supplementary Figure 11. Comparison of calculated peak temperatures as determined by solving the governing differential equation (Supplementary Equation 4.1) based on I(x) at 550

nm, versus those from fitting the full Planck spectrum near the ribbon centerline. The calculations were performed using the best-fit values of the power law exponent, *n*, for both the right and left conduction shoulders for each of the six Joule heating currents. The black dashed line is a one-to-one correspondence between these two sets of values. All the points lie close to this line, which indicates reasonably good agreement between the two approaches. Error bars based on the range of fitted values for *n* are included, but are too small to be visually observed in the plot.

c) Fitting for the $\kappa_{ph,HighT}(T)$ Power Law Exponent

We define the width of the "conduction shoulder", $w_{Shoulder}$, as the distance from the edge of the sample to the location where the temperature has increased to 90% of its peak value. Since the experimental intensity profiles are somewhat asymmetrical, which we attribute to a slightly non-uniform sample thickness, we consider the right and left conduction shoulders separately. From the camera images we are able to determine the conduction shoulder width with a precision of approximately 100 μm, limited by noise in the experimental data, which is smoothed using a ten-point moving average filter.

We fit the unknown power law exponent *n* in our expression to determine the phonon thermal conductivity above 630 K [i.e. $\kappa_{ph,HighT}(T) = \kappa_{ph,630\,\mathrm{K}} \cdot \left(\frac{T}{630\,\mathrm{K}} \right)^n$] by adjusting *n* until the measured and modeled conduction shoulders match within a specific margin of error. This margin of error is set by the level of precision of the conduction shoulders in the experimental intensity profiles, namely, $\delta w_{Shoulder} \approx \pm 100$ μm. This fitting procedure is repeated for each of the six Joule heating currents as well as both the right and left conduction shoulders, which results in twelve values of *n*. These twelve *n* values, along with their error bars corresponding to $\delta w_{Shoulder}$, are shown in Supplementary Figure 12 as a function of the Joule heating current.

Supplementary Figure 13a below is similar to Fig. 4e of the main text but with some additional details showing the differences between left- and right-shoulder fits. The solid red and blue $\kappa_{ph,HighT}(T)$ curves in Supplementary Figure 13a are calculated using the mean values of the red and blue point sets in Supplementary Figure 12. In other words, the two curves represent an average of the fitted *n* values for the six different Joule heating currents, where the right and left

shoulders are treated separately. The shaded error bands associated with those curves show the values of *n* for one standard deviation above and below the average values for each shoulder. Meanwhile, the six cyan and six magenta points in Supplementary Figure 13a represent the thermal conductivity at the peak sample temperature calculated using the corresponding values of *n* (as indicated by the six red and six blue points in Supplementary Figure 12). In order to convey the uncertainty in $\kappa_{ph,HighT}(T)$, the shaded error bands that reflect the sensitivity of the modeled temperature profile to *n* is shown in Supplementary Figure 13(a). Supplementary Figure 13(b) shows the comparison of the experimental and modeled temperature profiles for the highest Joule heating input current, which results in a peak temperature of ~2290 K. The solid red lines show the temperature profile using separate best fit values of *n* for the right and left sides. Note that neither *n* = 0 nor the *n* = -1 assumptions can reproduce the plateau-like temperature profile measured experimentally (solid blue line), which might otherwise have been expected for a sample dominated by disorder or umklapp scattering, respectively. The blue dotted lines represent an extrapolation of the measured data at the ends of the RGO ribbon, where the incandescent signal falls below the noise floor of the camera. The best-fit high-*T* value of *n* is ~ -3, which indicates a stronger scattering effect compared to the classic umklapp behavior (n = -1).

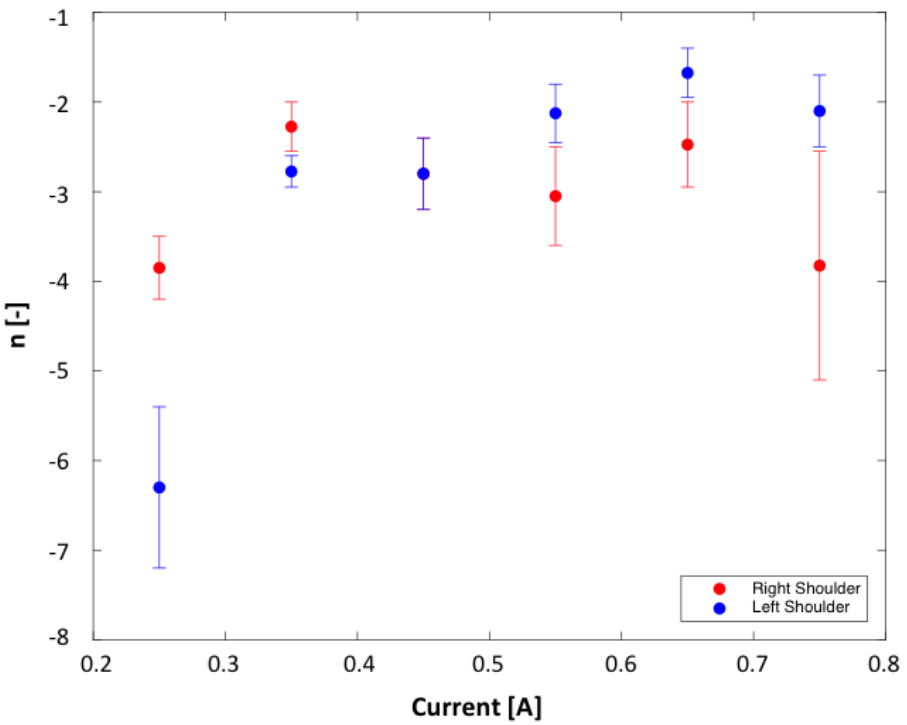

Supplementary Figure 12. The twelve best-fit values for the power law exponent *n* as a function of the Joule heating current. The mean and standard deviation of the fitted *n* values are 3.05 ± 0.67 and 2.96 ± 1.69 for the right and left shoulders, respectively. The error bars represent the degree to which the modeled value of *n* can be perturbed while still returning a conduction shoulder value that matches within a ±100 μm margin of error.

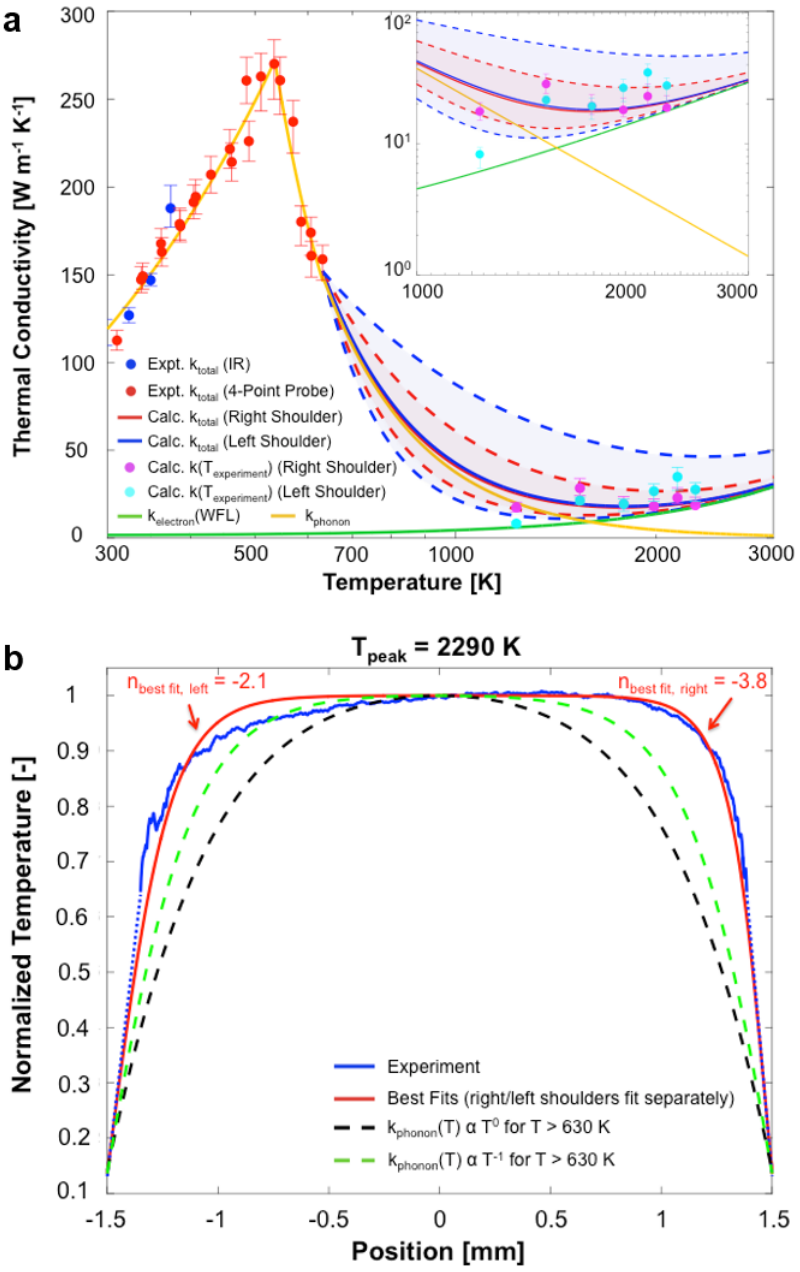

Supplementary Figure 13. (a) Experimental and modeled thermal conductivity as a function of temperature between 300 K and 3000 K. (b) Comparison of the experimental and modeled temperature profiles for the highest Joule heating input current, resulting in a peak temperature of ~2290 K. The shaded error bands indicate the values of *n* for one standard deviation above and below the average values for each shoulder.